Voltage-controlled long-range propagation of indirect excitons in a van der Waals heterostructure

L. H. Fowler-Gerace, D. J. Choksy, and L. V. Butov
Department of Physics, University of California at San Diego, La Jolla, California 92093, USA

(Received 15 January 2021; accepted 23 September 2021; published 8 October 2021)

Indirect excitons (IXs), also known as interlayer excitons, can form the medium for excitonic devices whose operation is based on controlled propagation of excitons. A proof of principle for excitonic devices was demonstrated in GaAs heterostructures where the operation of excitonic devices is limited to low temperatures. IXs in van der Waals transition-metal dichalcogenide (TMD) heterostructures are characterized by high binding energies making IXs robust at room temperature and offering an opportunity to create excitonic devices operating at high temperatures suitable for applications. However, a characteristic feature of TMD heterostructures is the presence of moiré superlattice potentials, which are predicted to cause modulations of IX energy reaching tens of meV. These in-plane energy landscapes can lead to IX localization, making IX propagation fundamentally different in TMD and GaAs heterostructures and making uncertain whether long-range IX propagation, sufficiently long to allow for creating elaborate excitonic devices and circuits, can be realized in TMD heterostructures. In this work, we realize long-range IX propagation with the $1/e$ IX luminescence decay distances reaching 13 microns in a $MoSe_2/WSe_2$ heterostructure. We trace the IX luminescence along the IX propagation path. In the presented TMD materials, the long-range IX propagation occurs up to ~50 K. This is a step toward the room temperature operation, which can be realized in TMD heterostructures due to the high IX binding energy. We also realize control of the long-range IX propagation by voltage. The IX luminescence signal in the drain of an excitonic transistor is controlled within 40 times by gate voltage. The control of the IX propagation in the $MoSe_2/WSe_2$ heterostructure is governed by new mechanisms, beyond the mechanism for controlling IX transport by an energy barrier to IX propagation (or a trap for IXs) created by the gate electrode, known since the studies of GaAs heterostructures. We discuss the origin of the voltage-controlled long-range IX propagation in the $MoSe_2/WSe_2$ heterostructure, in particular, the electric-field control of the moiré potential.

DOI: 10.1103/PhysRevB.104.165302

I. INTRODUCTION

Spatially indirect excitons (IXs) are formed by electrons and holes confined in separated layers. The separation between the electron and hole layers allows for controlling the overlap of electron and hole wave functions and achieving long IX lifetimes, orders of magnitude longer than lifetimes of spatially direct excitons (DXs) [1]. The long IX lifetimes allow them to travel over long distances before recombination [2–11].

IXs have built-in dipole moments ed (d is the separation between the electron and hole layers) and their energy can be controlled by voltage: Gate voltage V_g controls the electric field normal to the layers $F_z \propto V_g$ and changes the IX energy by edF_z. This allows for creating tailored in-plane potential landscapes for IXs $E(x, y) = -edF_z(x, y)$ and controlling them *in situ* by voltage $V_g(x, y)$. The possibility to control IX energy by voltage and the ability of IXs to propagate over long distances led to the realization of a variety of tailored voltage-controlled in-plane potential landscapes, which are explored in studies of IX transport. These landscapes include excitonic ramps [2,6], excitonic lattices [12–14], excitonic narrow channels [15,16], excitonic conveyers [17], and excitonic split gate devices [18].

IX devices are also explored for developing signal processing based on the exciton dipole, which is a novel computational state variable, different from established computational state variables such as electron charge in electronic devices. Potential advantages of excitonic devices include energy-efficient signal processing and seamless coupling to optical communication [11]. Experimental proof of principle was demonstrated for excitonic transistors [19,20].

The realization of excitonic devices, whose operation is based on controlled propagation of excitons, relies on meeting the requirements of (i) long-range IX propagation over lengths exceeding the in-plane dimensions of excitonic devices and (ii) *in situ* control of IX propagation, in particular, by voltage. These requirements were met with IXs in GaAs heterostructures and the studies outlined above used the GaAs platform.

However, excitons exist at temperatures roughly below E_{ex}/k_B (E_{ex} the exciton binding energy, k_B the Boltzmann constant) [21] and, due to their low binding energies, IXs in GaAs heterostructures exist at low temperatures. E_{ex} is typically ~4 meV in GaAs/AlGaAs heterostructures [22] and achieves ~10 meV in GaAs/AlAs heterostructures [23]. The proof of principle for the operation of IX switching devices based on voltage-controlled IX propagation was demonstrated up to ~100 K in GaAs heterostructures [20]. IX devices based on controlled IX propagation are also explored in GaN/AlGaN heterostructures with high E_{ex} reaching ~30 meV [24].

Van der Waals heterostructures composed of atomically thin layers of transition-metal dichalcogenides (TMDs) [25] allow the realization of excitons with high binding energies [26,27]. IXs in TMD heterostructures are characterized by binding energies reaching hundreds of meV [28,29] making them stable at room temperature [30]. Due to the high IX binding energy, TMD heterostructures can form a material platform for creating excitonic devices operating at high temperatures suitable for applications.

However, in contrast to GaAs heterostructures, a characteristic feature of TMD heterostructures is the presence of significant moiré superlattice potentials, which are predicted to cause modulations of IX energy reaching tens of meV in mechanically stacked TMD heterostructures with adjacent electron and hole layers and a small angle $\delta\theta$ between the layers, such as the studied $MoSe_2/WSe_2$ heterostructure [31–34]. Strong variations of the interlayer band gap within the moiré supercell, Δ, causing the modulations of IX energy were predicted for these TMD heterostructures with both R (AA, $\sim 0^\circ$ twist) and H (AB, $\sim 60^\circ$ twist) stacking $\Delta \sim 100$ (90) and 25 (17) meV for $MoSe_2/WSe_2$ heterobilayers with R and H stacking, respectively, in Ref. [34] (in Ref. [31]). Large Δ were also predicted for other TMD heterostructures of this type [31,34]. A spatial modulation of the local band gap with an amplitude of 150 meV was reported in scanning tunneling microscopy measurements and calculations of a rotationally aligned MoS_2/WSe_2 heterobilayer [35]. The moiré superlattice period $b \approx a/\sqrt{\delta\theta^2 + \delta^2}$ is typically in the $\sim$10 nm range (a is the lattice constant, δ is the lattice mismatch, $\delta\theta$ is the twist angle deviation from $n\pi/3$, n is an integer) [36,37].

This prediction inspired extensive experimental studies. For instance, the moiré superlattices were considered as the origin of splitting of IX luminescence to two or more lines [38–44]. In these works, the strong modulations of IX energy in the moiré potentials were, in particular, evidenced by wide spreads of luminescence line energies of excitons localized in the moiré potential minima. Four (five) luminescence lines spread over $\sim$70 (100) meV in $MoSe_2/WSe_2$ with 1° (2°) twist were discussed in terms of exciton states localized in a moiré potential of $\sim$150 meV [41]. Multiple narrow luminescence lines were spread over $\sim$30 meV in $MoSe_2/WSe_2$ with 2° twist and $\sim$20 (30) meV in $MoSe_2/WSe_2$ with 60° (56°) twist [40]. WSe_2 absorption resonances spread over $\sim$100 meV in both R- and H-stacked WSe_2/WS_2 were discussed in terms of a peak-to-peak exciton moiré potential of 250 meV [42].

We note however that there are other interpretations of the splitting of IX luminescence lines, including excitonic states split due to the conduction band K-valley spin splitting [45], excitonic states indirect in momentum space and split due to the valley energy difference [46,47] or spin-orbit coupling [48], and neutral and charged IX states [49]. We considered the origin of splitting of IX luminescence to two lines in Ref. [49].

The predicted strong moiré superlattice potentials in TMD heterostructures should have a significant effect on exciton propagation. The strong in-plane energy landscapes can lead to IX localization, making IX propagation fundamentally different in TMD and GaAs heterostructures and making uncertain whether long-range IX propagation can be realized in principle in TMD heterostructures with moiré superlattice potentials.

Propagation of both DXs in TMD monolayers [50–55] and IXs in TMD heterostructures [56–61] is intensively studied. A relatively short-range IX propagation with $1/e$ IX luminescence decay distances reaching ~ 3 μm [56–60], control of IX propagation by voltage within these distances [58,59], and control of DX luminescence by voltage up to 5 μm away from the generation spot [61] were reported in TMD heterostructures.

The extent to which the moiré superlattice potentials affect the IX diffusivity is not fully established. The comparison of $MoSe_2/WSe_2$ heterostructures with $MoSe_2/hBN/WSe_2$ heterostructures, where the moiré superlattice potential is suppressed by an hBN spacer between the $MoSe_2$ and WSe_2 layers, evidences the reduction of IX propagation due to moiré superlattice potentials: the IX propagation with the $1/e$ decay distance up to 2.6 μm was observed in $MoSe_2/hBN/WSe_2$ and shorter IX propagation with the $1/e$ decay distance beyond the laser spot below 1 μm was observed in $MoSe_2/WSe_2$ [58].

In this work, we realize in a $MoSe_2/WSe_2$ TMD heterostructure IX propagation with the $1/e$ IX luminescence decay distance $d_{1/e} \sim 13$ μm. This long propagation distance exceeds $d_{1/e} \sim 3$ μm realized in the earlier studies of TMD heterostructures [56–60] and is sufficiently long to allow for creating elaborate excitonic devices and circuits within the IX propagation length that is required for performing operations with IX fluxes [19,20]. In the presented TMD materials, the long-range IX propagation occurs up to $\sim$50 K. This is a step toward the room temperature operation, which can be realized in TMD heterostructures due to the high IX binding energy. We also realize control of the long-range IX propagation by voltage. The control of the IX propagation in the $MoSe_2/WSe_2$ heterostructure is governed by new mechanisms, beyond the known mechanism for controlling IX transport by an energy barrier to IX propagation (or a trap for IXs) created by the gate electrode that was reported in the studies of GaAs [19,20] and TMD [58,59] heterostructures. We discuss the origin of the voltage-controlled long-range IX propagation in the $MoSe_2/WSe_2$ heterostructure, in particular, the electric-field control of the moiré potential. The control of moiré superlattice potentials by voltage can be used in various applications ranging from excitonic devices outlined in this work to quantum simulators and quantum emitter arrays based on moiré superlattices [34,62,63].

II. EXPERIMENT

The $MoSe_2/WSe_2$ heterostructure is assembled by stacking mechanically exfoliated 2D crystals on a graphite substrate. The $MoSe_2$ and WSe_2 monolayers are encapsulated by hexagonal boron nitride (hBN) serving as dielectric cladding layers. The energy-band diagram is schematically shown in Fig. 1(a). IXs are formed from electrons and holes confined in adjacent $MoSe_2$ and WSe_2 monolayers, respectively. The lowest energy DX state is optically active in $MoSe_2$ and dark in WSe_2, and the lowest energy IX state is optically active [31,32,64–68]. The bias across the heterostructure is created by the gate voltage V_g applied between the narrow

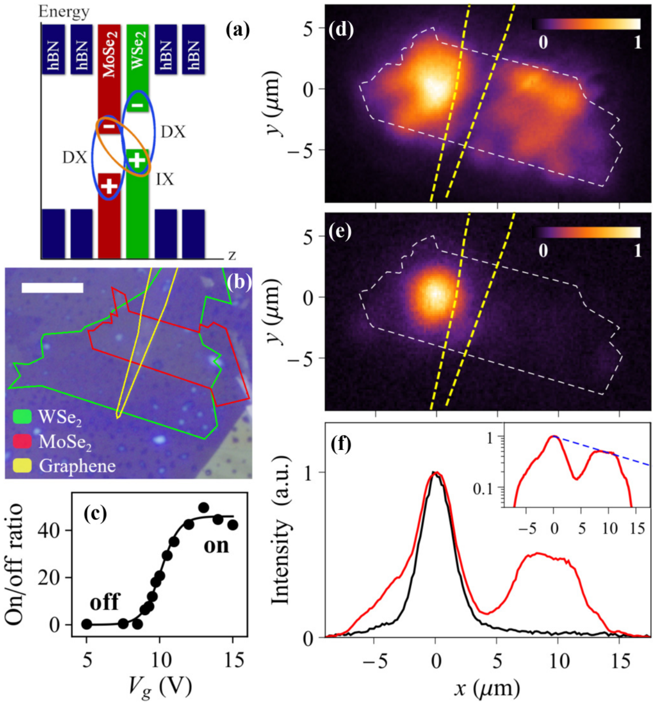

FIG. 1. Voltage-controlled IX propagation. (a) Band diagram of van der Waals MoSe$_2$/WSe$_2$ heterostructure. The ovals indicate a direct exciton (DX) and an indirect exciton (IX) composed of an electron (−) and a hole (+). (b) Microscope image showing the layer pattern of the device; scale bar is 10 μm. The green, red, and yellow lines indicate the boundaries of the WSe$_2$ and MoSe$_2$ monolayers and graphene gate, respectively. (d), (e) x-y images of IX luminescence in the on (d) and off (e) state of the excitonic transistor. The white and yellow dashed lines show the boundary of the MoSe$_2$/WSe$_2$ heterostructure and graphene gate, respectively. The gate voltage V_g controls the IX propagation from the laser excitation spot at $x = 0$ (the source) to the other side of the graphene gate $x \gtrsim 6$ μm (the drain). $V_g = 10$ V (d), 0 (e). (f) Normalized IX luminescence profiles along $y = 0$ for the images in (d) and (e) shown by the red and black lines, respectively. Inset shows the same IX luminescence profile in the on state on log scale. For comparison, dashed line shows exponential signal reduction with $1/e$ decay distance 13 μm. A lower IX luminescence intensity is seen in the region covered by the graphene gate, which is centered at $x = 4$ μm. (c) Total IX luminescence intensity in the drain (integrated over $x = 6$–13 μm) vs V_g. For all data, $P_{ex} = 4$ mW, $T = 1.7$ K.

semitransparent multilayer graphene top gate [Fig. 1(b)] and the global graphite back gate.

The graphene gate is centered at $x = 4$ μm [Figs. 1(d)–1(f)]. The heterostructure region to the left of the gate ($x = -7$ to 2 μm) is referred to as the source and the heterostructure region to the right of the gate ($x = 6$ to 13 μm) is referred to as the drain. IXs are optically generated by laser excitation focused in the source region.

When the device is in the off state, IX propagation from the source to the drain is suppressed and the IX luminescence profile follows the laser excitation profile [Fig. 1(e)]. When the device is switched on, IXs spread out away from the laser excitation spot and propagate to the drain region [Fig. 1(d)].

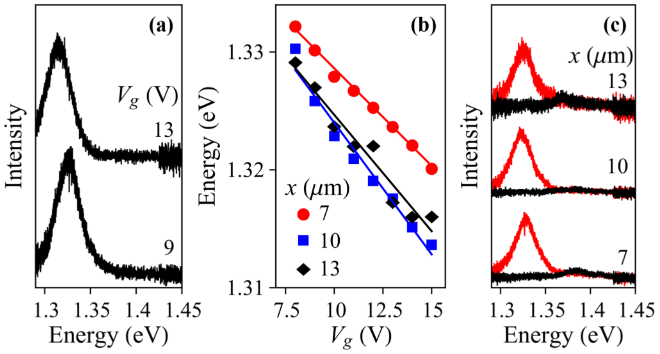

FIG. 2. Voltage-controlled IX energy. Tracing IX luminescence along IX propagation. (a) IX luminescence spectra at $x = 13$ μm for gate voltages $V_g = 9$ and 13 V. (b) IX energy vs V_g for positions in the drain region $x = 7$, 10, and 13 μm. (c) IX spectra in on (red) and off (black) state of the excitonic transistor for positions in the drain region $x = 7$, 10, and 13 μm. $V_g = 10$ V (on), 8.5 V (off). For all data, $P_{ex} = 4$ mW, $T = 1.7$ K.

Figure 1(f) shows IX luminescence profiles along $y = 0$ for the images in Figs. 1(d) and 1(e). The inset shows the same IX luminescence profile for the on state on log scale. For comparison, the dashed line shows exponential signal reduction with the $1/e$ decay distance 13 μm. A lower IX luminescence intensity is seen in the region covered by the graphene gate. The total IX luminescence intensity in the drain region (integrated over $x = 6$–13 μm) increases by 40 times as the gate voltage switches from off to on [Fig. 1(c)]. Figures 1(c)–1(f) present voltage-controlled long-range propagation of IXs in MoSe$_2$/WSe$_2$ heterostructures.

Next, we verify whether the propagating luminescence signal corresponds to the IX luminescence. Figures 2(a) and 2(b) show that at voltages that allow for IX propagation across the sample, the exciton luminescence energy is controlled by voltage in the entire drain region. This exhibits the basic IX property—IX energy control by voltage, outlined in the introduction. Figure 2(c) presents tracing the IX luminescence along the IX propagation path all the way up to the heterostructure edge ∼13 μm away from the region of IX optical generation. Figure 2(c) also shows that IX luminescence spectra at the drain demonstrate effective switching behavior between the off (black spectra) and on (red spectra) state. Tracing the IX luminescence along the IX propagation path with $1/e$ IX luminescence decay distance 13 μm and controlling IX propagation by voltage present the direct measurement of long-range IX propagation and excitonic transistor action in TMD heterostructures.

The IX luminescence spectra are traced over the drain region at different excitation powers P_{ex} [Figs. 3(a), 3(b)]. The total IX luminescence intensity in the drain increases with P_{ex} [Fig. 3(c)]. The IX propagation enhances with excitation power. Maximum IX propagation with $d_{1/e} \sim 13$ μm is realized at $P_{ex} \sim 1$ mW. Comparable P_{ex} were explored in the studies of TMD heterostructures where $d_{1/e} \sim 3$ μm was realized [57,58].

Figure 3(d) shows the optically measured IX energy along the IX propagation path. The overall IX energy reduction is observed (i) with increasing separation from the IX optical

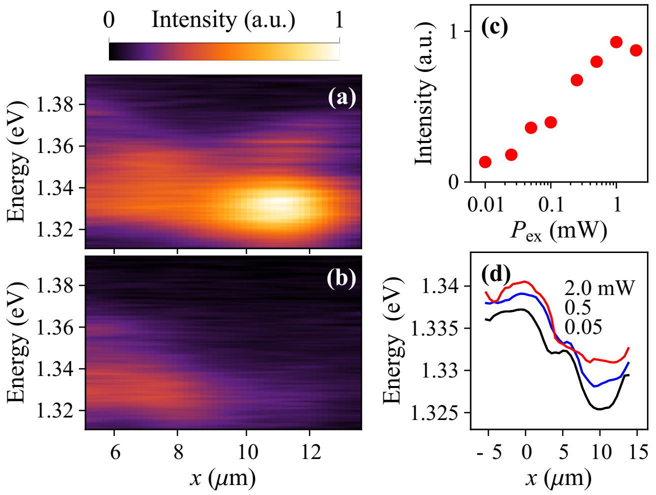

FIG. 3. Excitation power dependence of IX propagation. (a), (b) x-energy images of IX luminescence in the drain region for $P_{ex} =$ 2 mW (a) and 0.05 mW (b). (c) Total IX luminescence intensity in the drain (integrated over $x = 6$–13 μm) vs P_{ex}. (d) IX energy vs position for $P_{ex} = 0.05$ (black), 0.5 (blue), and 2 (red) mW. For all data, $V_g = 10$ V, $T = 1.7$ K.

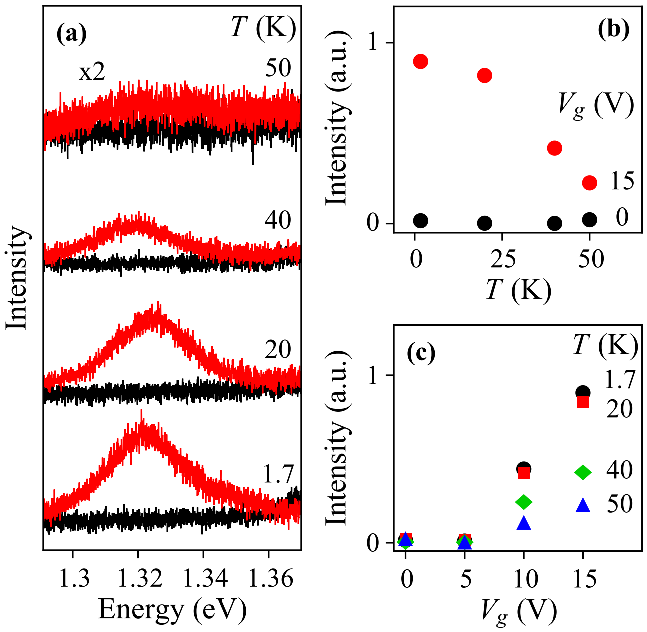

FIG. 4. Temperature dependence. (a) IX luminescence spectra in the drain at $x = 13$ μm at temperatures $T = 1.7$, 20, 40, and 50 K in on (red) and off (black) state of the excitonic transistor. $V_g = 15$ V (on) and 0 (off). (b) Total IX luminescence intensity in the drain (integrated over $x = 6$–13 μm) vs temperature in on ($V_g = 15$ V) and off ($V_g = 0$) state. (c) Total IX luminescence intensity in the drain (integrated over $x = 6$–13 μm) vs V_g for temperatures $T = 1.7$, 20, 40, and 50 K. For all data, $P_{ex} = 4$ mW.

generation spot and (ii) with reducing P_{ex}. Both indicate a reduction of IX energy with the reduced IX density. This is consistent with the repulsive interaction between IXs, which are dipoles oriented normal to the layers. Similar reduction of IX energy with increasing separation from the optical generation spot or with reducing P_{ex} is also characteristic of IXs in GaAs heterostructures and is explained in terms of the repulsive interaction between IX dipoles [5]. The local IX energy variations in the range of a few meV [Fig. 3(d)] are likely caused by the lateral potential landscape across the heterostructure. The IX energy variations due to the moiré superlattice have the period in the ~10 nm range [36,37]; these short-range energy variations are not resolved in the optical experiment with resolution 1.5 μm.

Figure 4 presents the temperature dependence of IX propagation. The long-range IX propagation through the drain region and the switching between on and off state are observed up to approximately 50 K.

III. DISCUSSION

The phenomenological properties of voltage-controlled long-range IX propagation in $MoSe_2/WSe_2$, outlined above, are qualitatively different from those in GaAs heterostructures [19,20]. GaAs/AlAs heterostructures, where IXs are formed from electrons and holes confined in adjacent AlAs and GaAs layers, respectively, have a staggered band alignment [20,23] similar to $MoSe_2/WSe_2$ heterostructures [Fig. 1(a)]. This makes GaAs/AlAs heterostructures a more close system for the comparison with $MoSe_2/WSe_2$ heterostructures. For the excitation spot positioned in the source region, similar to the experimental geometry in Fig. 1, in the GaAs/AlAs heterostructures IX propagation is long range at $V_g = 0$ while both a positive and negative voltage on a gate creating a barrier and a trap for IXs, respectively, suppress the IX propagation [20]. This behavior is opposite to the voltage-controlled IX propagation in $MoSe_2/WSe_2$ where applied voltage strongly enhances the IX propagation (Fig. 1).

The opposite behavior is also observed for the excitation spot positioned on the gate electrode. For the GaAs/AlAs heterostructures, trapping (antitrapping) IX potentials created by gate voltage cause the IX cloud confinement in (spreading away from) the gate region [20]. For the $MoSe_2/WSe_2$ heterostructure, the IX energy reduces with increasing V_g that facilitates trapping IXs in the gate region. However, similar to the case of excitation in the source region (Fig. 1), an enhancement of the IX propagation away from the excitation spot with increasing V_g is observed in the case of excitation in the gate region (Fig. 5).

In GaAs heterostructures, the IX propagation has been controlled by an energy barrier to IX propagation (or a trap for IXs) created by the gate electrode [19,20]. The control of IX transport realized in TMD heterostructures was referred to the same mechanism [58,59]. The qualitative differences outlined above show that the IX long-range propagation in the $MoSe_2/WSe_2$ heterostructure is controlled by a new mechanism, different from the control by an energy barrier or a trap for IXs created by the gate electrode.

This new mechanism enables the long-range IX propagation away from the excitation spot not only through the gate but everywhere in the plane of the heterostructure: Figs. 1(d)–1(f) show that increasing V_g enables the IX propagation away from the excitation spot both through the gate (toward positive x) and in the opposite direction (toward

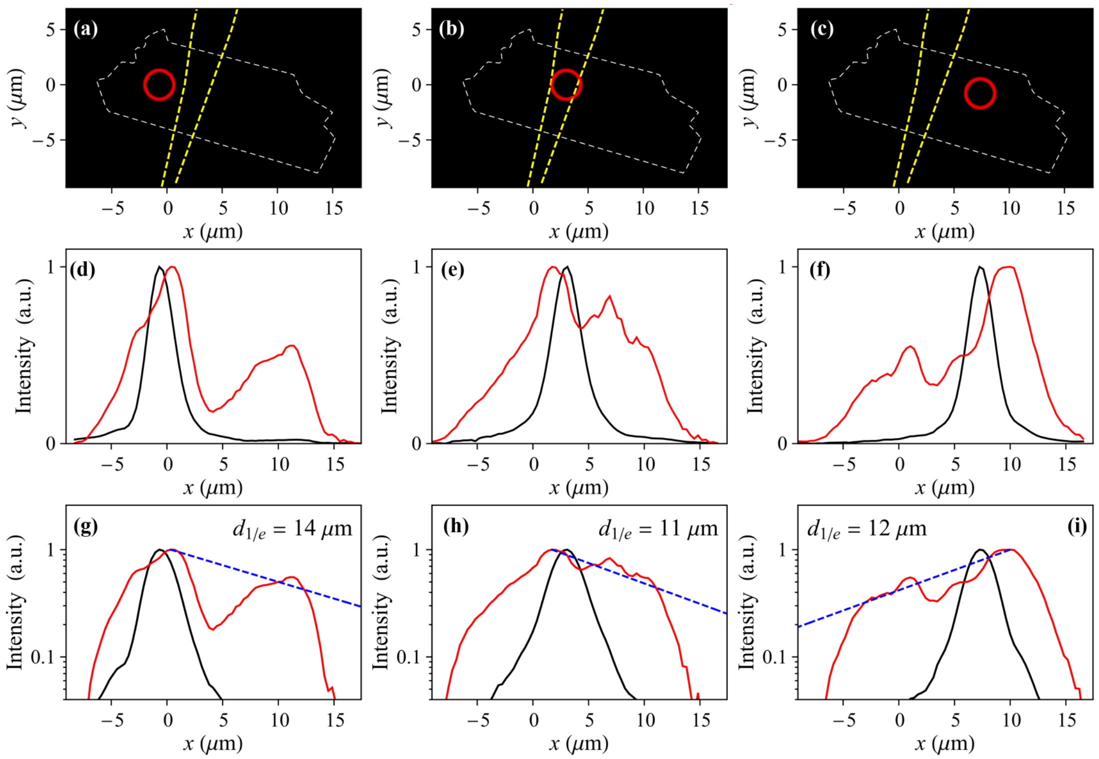

FIG. 5. Voltage-controlled IX propagation. (a)–(c) The white and yellow dashed lines show the boundaries of $MoSe_2/WSe_2$ heterostructure and graphene gate, respectively. The laser excitation spot [red circle in (a)–(c)] is positioned at the source [(a), (d), (g)], gate [(b), (e), (h)], and drain [(c), (f), (i)] region of the device. The gate voltage V_g controls the IX propagation from the laser excitation spot. (d)–(f) Normalized IX luminescence profiles along $y = 0$ for $V_g = 10$ V (red lines) and 0 (black lines). (g)–(i) Same IX luminescence profiles on log scale. For comparison with the IX luminescence profiles at $V_g = 10$ V, dashed lines show exponential signal reduction with $1/e$ decay distance $d_{1/e} = 14$, 11, and 12 μm, respectively. A lower IX luminescence intensity is seen in the region covered by the graphene gate, which is centered at $x = 4$ μm. For all data, $P_{ex} = 4$ mW, $T = 1.7$ K.

negative x); Fig. 5 shows that increasing V_g enables the IX propagation away from the excitation spot for any excitation spot position on the heterostructure.

The predicted strong moiré superlattice potentials [31–34] in the studied $MoSe_2/WSe_2$ heterostructure are expected to localize IXs and, therefore, the existence of the long-range IX propagation is nontrivial. Identifying the mechanism that can lead to the voltage-controlled long-range IX propagation in the heterostructures with the predicted moiré superlattice potentials forms the challenge for theoretical investigations. The relevant experimental data and possible origin of the voltage-controlled long-range IX propagation in the $MoSe_2/WSe_2$ heterostructure are discussed below.

IXs are the lowest energy exciton state in $MoSe_2/WSe_2$ heterostructures even at no applied voltage [Fig. 1(a)]. The absence of long-range IX propagation at $V_g = 0$ indicates IX localization. As outlined above, the moiré superlattice potentials are predicted to cause modulations of exciton energy reaching tens of meV [31–34] and these strong energy modulations can lead to the exciton localization.

The regime of long-range IX propagation is realized at $V_g \gtrsim 8$ V [Figs. 1(c), 1(d)]. The applied electric field can tune the moiré potential and cause the long-range IX propagation. The theory [34] predicts that the moiré potential is tuned by voltage in both R- and H-stacked TMD heterostructures. In particular, increasing electric field can reduce the moiré potential amplitude and can energetically align the potential energy minima at different sites of the moiré supercell, thus causing percolation of IX states through the structure [34]. The tuning of the moiré potential can cause the observed long-range IX propagation with applied electric field. The calculated electric field corresponding to the IX percolation is in the range of a few tenths of V/nm [34]. This is of the same order of magnitude with the estimated electric field for the onset of IX propagation in the studied device: $V_g = 8$ V creates electric field ~0.1 V/nm. We note however that a comparison with the theory can be complicated by factors including a possible built-in electric field [30], trion formation [49], moiré-site-dependent exciton binding energy and dipole moment [34], and atomic reconstruction, which can change the potential landscape and can create a network of propagation channels [69–73].

Besides the moiré potential, samples have disorder potential due to the heterostructure imperfections. The disorder potential also contributes to the IX localization and suppresses the IX propagation. The long-range IX propagation requires samples with a small disorder. The long-range propagation indicates the small disorder for IX transport scattering in the studied device.

In the regime of long-range IX propagation, $V_g \gtrsim 8$ V, the IX energy in the drain is effectively controlled by voltage applied to the graphene electrode (Fig. 2). This indicates that

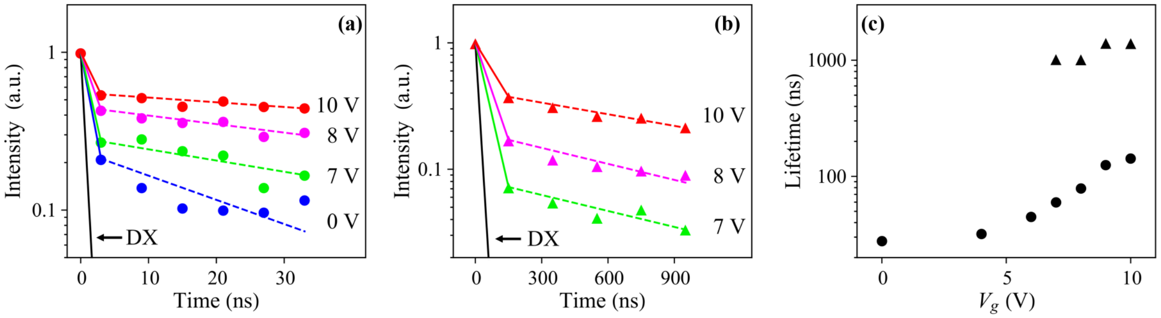

FIG. 6. IX luminescence decay. (a), (b) Decay of IX luminescence measured at the IX line energies 1.24–1.38 eV at short (a) and long (b) delay times vs voltage. This energy range corresponds to the IX state showing the long-range propagation (Fig. 2). For the data in (a), the laser excitation pulse duration $\tau_{\text{pulse}} = 14$ ns, period $\tau_{\text{period}} = 60$ ns, and edge sharpness ~0.5 ns and the signal integration window $\tau_{\text{w}} = 6$ ns. For the data in (b), to access the long delay times τ_{pulse}, τ_{period}, and τ_{w} are increased to 400, 1600, and 200 ns, respectively. (c) IX luminescence decay times at short (points) and long (triangles) delay times derived from the data (a) and (b), respectively. The IX luminescence is integrated over the entire heterostructure to increase the signal. For all data, $P_{\text{ex}} = 4$ mW, $T = 1.7$ K.

voltage applied to the graphene electrode laterally extends beyond the region of the graphene electrode over the entire heterostructure. This extension, in turn, indicates that the heterostructure acquires metallic conductivity. The metallization may contribute to screening of in-plane potential landscapes, facilitating the long-range IX propagation.

The metallization may also be related to the tuning of moiré potential by applied electric field. No intentional sample doping was done for the studied heterostructure; however, unintentional *n*-type doping is typical for TMD layers [76]. In the studied sample, the estimated electron concentration $n_{\text{B}} \sim 2 \times 10^{11}$ cm^{-2} [49]. Delocalization of electrons and/or charged IXs due to the tuning of moiré potential by electric field can cause the metallization.

The IX propagation is enhanced at higher excitation powers. A similar behavior is observed for IXs in GaAs heterostructures [5]. IXs are out-of-plane dipoles, which interact repulsively. The repulsive interaction between IXs contributes to screening of in-plane potential landscapes. Furthermore, due to the repulsive interaction, the IX energy increases with density and, as a result, is higher in the region of IX generation [Fig. 3(d)]. This results in IX drift away from the excitation region. Both enhanced screening of in-plane potentials and drift enhance the IX propagation with increasing density [5].

Increasing V_{g} also increases the IX lifetime (Fig. 6). The increase of IX lifetime contributes to the enhancement of IX propagation with voltage. The IX diffusion coefficient D can be estimated from the IX propagation length l and IX lifetime τ as $D \sim l^2/\tau$. For $l \sim 10$ μm corresponding to the IX propagation length (Fig. 1) and $\tau \sim 1$ μs corresponding to the IX luminescence decay time at long delay times (Fig. 6) at $V_{\text{g}} = 10$ V, the estimate gives $D \sim 1$ cm^2/s.

This work presents the proof of principle to overcome moiré superlattice potentials and realize the long-range IX propagation in $MoSe_2/WSe_2$ TMD heterostructures that make TMD a promising materials platform for the development of excitonic devices. The IX binding energies are high enough to make the IXs stable at room temperature and IXs in the laser excitation spot are observed at room temperature in $MoSe_2/WSe_2$ heterostructures [49]. However, the long-range IX propagation and the switching between the on and off state are observed up to ~50 K in the studied heterostructure (Fig. 4), presumably due to the heterostructure imperfections. The realization of long-range IX propagation at higher temperatures is the subject for future works.

IV. CONCLUSION

In summary, we realize long-range IX propagation with the $1/e$ IX luminescence decay distances reaching 13 microns in a $MoSe_2/WSe_2$ heterostructure. This propagation distance is sufficiently long to allow for creating elaborate excitonic devices and circuits. We also realize control of the long-range IX propagation by gate voltage. The control of the IX propagation in the $MoSe_2/WSe_2$ heterostructure is governed by new mechanisms, beyond the known mechanism for controlling IX transport by an energy barrier to IX propagation (or a trap for IXs) created by the gate electrode that was reported in GaAs and TMD heterostructures. We discuss the origin of the voltage-controlled long-range IX propagation in the $MoSe_2/WSe_2$ heterostructure, in particular, the electric-field control of the moiré potential.

ACKNOWLEDGMENTS

We thank E. V. Calman, M. M. Fogler, D. E. Nikonov, I. A. Young, S. Hu, A. Mishchenko, and A. K. Geim for valuable discussions and contributions at the earlier stage of studies of IXs in TMD heterostructures. These studies were supported by DOE Office of Basic Energy Sciences under Award No. DE-FG02-07ER46449. The heterostructure fabrication and data analysis were supported by SRC and NSF Grant No. 1905478.

APPENDIX A: IX PROPAGATION FOR DIFFERENT EXCITATION SPOT POSITIONS

The voltage-controlled long-range IX propagation is observed for the laser excitation spot positioned in the source, gate, or drain regions (Fig. 5). In all these three cases, switching on the exciton propagation by applied voltage extends IXs over the entire $MoSe_2/WSe_2$ heterostructure and enhances the IX luminescence $1/e$ decay distance beyond 10 μm (Fig. 5).

APPENDIX B: IX LUMINESCENCE DECAY

The IX luminescence decay is nonexponential. We probe the faster initial decay [Fig. 6(a)] with the laser excitation pulse duration $\tau_{\mathrm{pulse}} = 14$ ns, period $\tau_{\mathrm{period}} = 60$ ns, and edge sharpness ~0.5 ns and the signal integration window $\tau_{\mathrm{w}} = 6$ ns. We probe a slower decay at long delay times with τ_{pulse}, τ_{period}, and τ_{w} increased to 400, 1600, and 200 ns, respectively. The IX luminescence decay times increase with V_{g} [Fig. 6(c)]. The DX decay closely follows the excitation laser decay indicating that the DX lifetime is shorter than the experimental resolution.

The IX luminescence decay time increase with V_{g} is in accord with the reduction of IX energy [Fig. 2(b)] further below the DX energy that reduces the overlap of the electron and hole wave functions for IXs [23]. The IX decay times are orders of magnitude longer than the DX decay times [74] and are controlled by gate voltage (Fig. 6). Different factors may contribute to deviations of the luminescence decay from an exponential decay. For instance, due to a possible heterostructure inhomogeneity the areas with shorter exciton lifetimes may contribute more at initial decay times. A fast initial component may also appear due to the decay of low-energy DX states, which appear in the IX spectral range due to the tail of DX density of states. Localized DXs at low energies in the spectral range of IXs were studied in GaAs/AlAs heterostructures [75].

APPENDIX C: OPTICAL MEASUREMENTS

In the cw experiments, excitons were generated by a cw HeNe laser with excitation energy $E_{\mathrm{ex}} = 1.96$ eV. Luminescence spectra were measured using a spectrometer with resolution 0.2 meV and a liquid-nitrogen-cooled CCD. The laser was focused to a spot size ~3.5 μm. The IX luminescence decay time was measured using a pulsed semiconductor laser with $E_{\mathrm{ex}} = 1.96$ eV; the emitted light was detected by a liquid-nitrogen-cooled CCD coupled to a PicoStar HR TauTec time-gated intensifier. The experiments were performed in a variable-temperature 4He cryostat.

APPENDIX D: THE HETEROSTRUCTURE FABRICATION AND CHARACTERIZATION

The studied van der Waals heterostructures were assembled using the dry-transfer peel-and-lift technique [76]. In brief, individual crystals of graphene, hBN, $\mathrm{MoSe_2}$, and $\mathrm{WSe_2}$ were first micromechanically exfoliated onto different Si substrates that were coated with a double polymer layer consisting of polymethyl glutarimide (PMGI) and polymethyl methacrylate (PMMA). The bottom PMGI was then dissolved with the tetramethylammonium hydroxide based solvent CD-26, causing the top PMMA membrane with the target 2D crystal to float on top of the solvent. The PMMA membrane functions both as a support substrate for transferring the crystal and as a barrier to protect the crystal from the solvent. Separately, a large graphite crystal was exfoliated onto an oxidized Si wafer, which later served as the bottom electrode. The PMMA membrane supporting the target crystal was then flipped over and aligned above an atomically flat region of the graphite crystal using a micromechanical transfer stage. The two crystals were brought into contact and the temperature of the stage was ramped to 80 °C in order to increase adhesion between the 2D crystals. Then, the PMMA membrane was slowly peeled off leaving the bilayer stack on the wafer. The procedure was repeated leading to a multicrystal stack with the desired layer sequence. No intentional sample doping was done; however, unintentional n-type doping is typical for TMD layers [76]. The thickness of bottom and top hBN layers is about 40 and 30 nm, respectively. The $\mathrm{MoSe_2}$ layer is on top of the $\mathrm{WSe_2}$ layer. The long $\mathrm{WSe_2}$ and $\mathrm{MoSe_2}$ edges reach ~30 and ~20 μm, respectively, which enables a rotational alignment between $\mathrm{WSe_2}$ and $\mathrm{MoSe_2}$ monolayers. The twist angle $\delta\theta = 0.5^\circ \pm 0.8^\circ$. The value of $\delta\theta$ is estimated from the angle between the long $\mathrm{WSe_2}$ and $\mathrm{MoSe_2}$ edges [Figs. 1(b) and 7]. The results and discussion in this work apply to both R and H (AA and AB) stacking; therefore we did not verify stacking in the sample. Our work shows that the long-range IX propagation can be realized in principle in TMD heterostructures with the predicted strong moiré superlattice potentials. The studies of sample statistics, and in particular, verifying the role of the rotational alignment between crystals on the IX propagation, is the subject for future works.

Photolithography was employed to define contact regions to graphene and graphite crystals, which followed by metal evaporation of electrical contacts (10 nm Ti / 300 nm Au). Liftoff and sample annealing were performed by immersing the lithographically patterned sample in Remover PG, an N-methyl-2-pyrrolidone (NMP) based solvent stripper, at 70 °C for 12 hours.

Figure 7 presents a microscope image showing the layer pattern of the device on an area larger than in Fig. 1(b). The layer boundaries are indicated. The hBN layers cover the entire areas of $\mathrm{MoSe_2}$, $\mathrm{WSe_2}$, and graphene layers so that there is no short electrical connection between either the top or the bottom gate and the $\mathrm{MoSe_2}$ and $\mathrm{WSe_2}$ layers of the heterostructure.

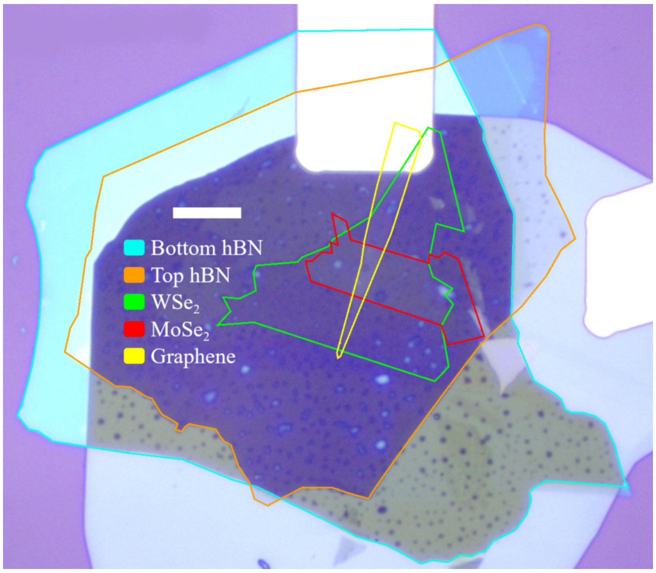

FIG. 7. The layer pattern. Microscope image showing the layer pattern of the device on an area larger than in Fig. 1(b). Scale bar is 10 μm. The green, red, yellow, cyan, and orange lines indicate the boundaries of $\mathrm{WSe_2}$ and $\mathrm{MoSe_2}$ monolayers, graphene gate, and bottom and top hBN layers, respectively.

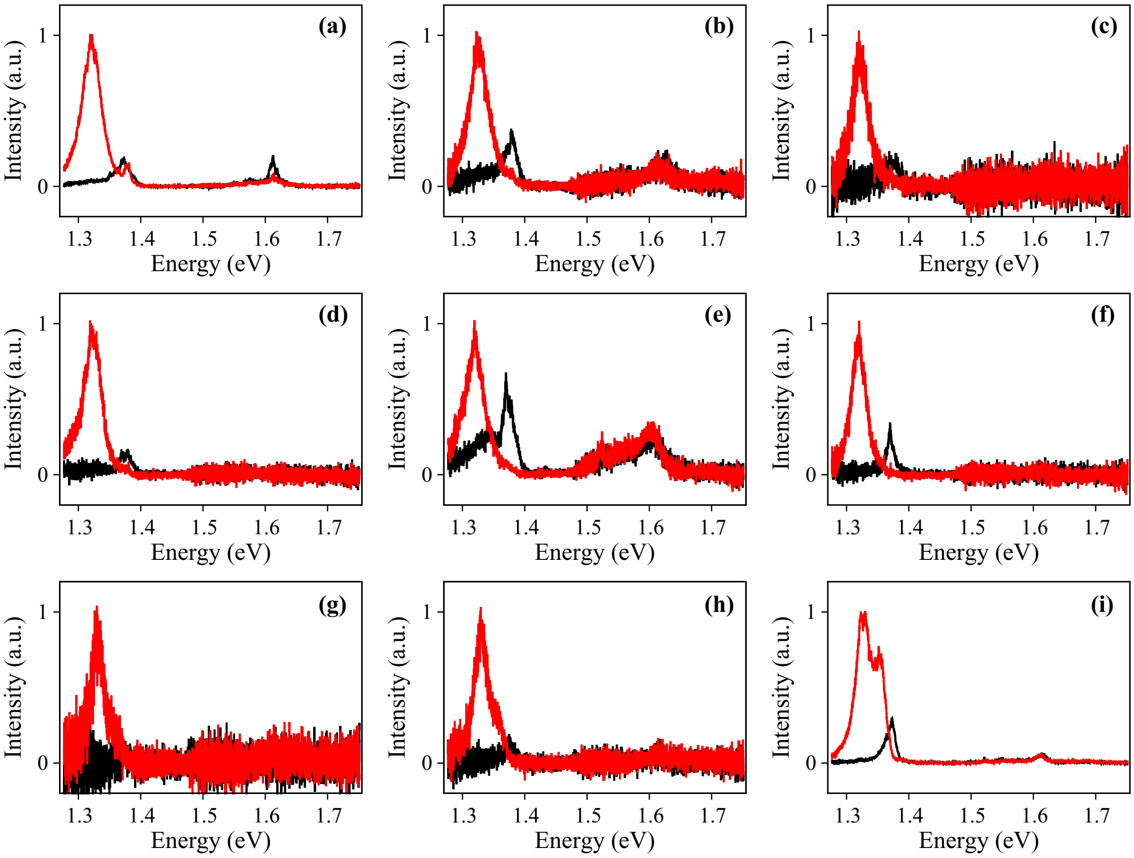

FIG. 8. Luminescence spectra for an extended spectral range. Luminescence spectra for an extended spectral range including the DX luminescence for excitation in the source [(a)–(c)], gate [(d)–(f)], and drain [(g)–(i)] at $x = 1, 4$, and 9 μm, respectively, measured in the source [(a), (d), (g)], gate [(b), (e), (h)], and drain [(c), (f), (i)] at $x = 0, 4$, and 9 μm, respectively, for gate voltages $V_g = 0$ and 10 V corresponding to the off (black) and on (red) state of the excitonic transistor. $P_{ex} = 0.05$ mW, $T = 1.7$ K.

The voltage was applied to the graphene top gate; the graphite back gate was grounded. The leakage current across the device in the on state reached ∼0.7 nA at the highest voltage (15 V) and excitation power (4 mW) in the experiment.

Luminescence spectra for an extended spectral range including the DX luminescence are presented in Fig. 8. Figure 8 shows the spectra under the graphene gate, on the source, and drain parts of the structure at gate voltages corresponding to the on and off states of the excitonic transistor.

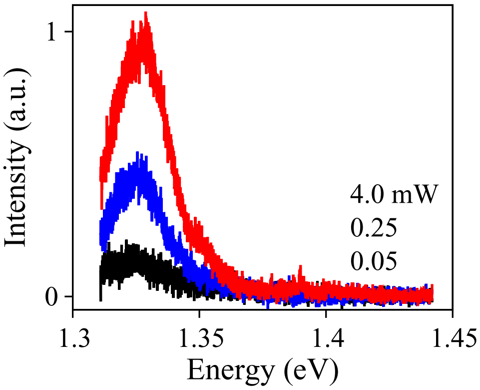

FIG. 9. Excitation power dependence. Luminescence spectra of propagating IXs at $x = 10$ μm for $P_{ex} = 0.05$, 0.25, and 4 mW. Excitation spot is at $x = 0$, $V_g = 10$ V, $T = 1.7$ K.

The luminescence spectra of propagating IXs are shown in Fig. 9 for different laser powers P_{ex}. The IX luminescence intensity increases and the spectrum shifts to higher energies with increasing P_{ex} (Fig. 9). An intensity increase and a

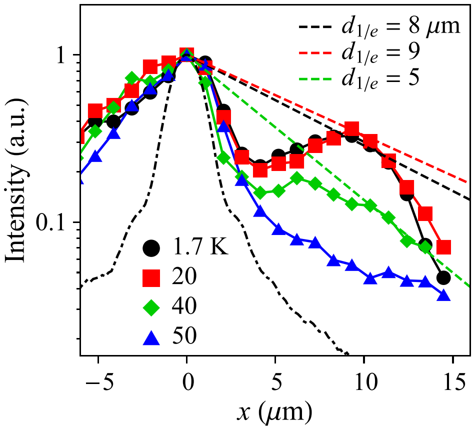

FIG. 10. Temperature dependence. Normalized profiles of luminescence of propagating IXs along $y = 0$ at $T = 1.7, 20, 40$, and 50 K. Dot-dashed line, which shows a normalized profile of DX luminescence in MoSe$_2$ at 50 K, presents the limit for the excitation spot extent. Dashed lines show exponential signal reduction with $1/e$ decay distance $d_{1/e} = 8, 9$, and 5 μm. $V_g = 10$ V, $P_{ex} = 4$ mW.

spectrum shift to higher energies are also presented in Fig. 3 and discussed in Sec. II.

The luminescence profiles of propagating IXs are shown in Fig. 10 for different temperatures. The IX propagation length presented by the $1/e$ decay distance $d_{1/e}$ reduces with increasing temperature (Fig. 10). A reduction of IX propagation with increasing temperature is also presented in Fig. 4 and discussed in Sec. III.

[1] Y. E. Lozovik and V. I. Yudson, A new mechanism for superconductivity: pairing between spatially separated electrons and holes, Zh. Eksp. Teor. Fiz. **71**, 738 (1976) [Sov. Phys. JETP **44**, 389 (1976)].

[2] M. Hagn, A. Zrenner, G. Böhm, and G. Weimann, Electric-field-induced exciton transport in coupled quantum well structures, Appl. Phys. Lett. **67**, 232 (1995).

[3] L. V. Butov, A. C. Gossard, and D. S. Chemla, Macroscopically ordered state in an exciton system, Nature (London) **418**, 751 (2002).

[4] Z. Vörös, R. Balili, D. W. Snoke, L. Pfeiffer, and K. West, Long-Distance Diffusion of Excitons in Double Quantum Well Structures, Phys. Rev. Lett. **94**, 226401 (2005).

[5] A. L. Ivanov, L. E. Smallwood, A. T. Hammack, Sen Yang, L. V. Butov, and A. C. Gossard, Origin of the inner ring in photoluminescence patterns of quantum well excitons, Europhys. Lett. **73**, 920 (2006).

[6] A. Gärtner, A. W. Holleitner, J. P. Kotthaus, and D. Schuh, Drift mobility of long-living excitons in coupled GaAs quantum wells, Appl. Phys. Lett. **89**, 052108 (2006).

[7] S. Lazić, P. V. Santos, and R. Hey, Exciton transport by moving strain dots in GaAs quantum wells, Phys. E (Amsterdam, Neth.) **42**, 2640 (2010).

[8] A. V. Gorbunov, V. B. Timofeev, and D. A. Demin, Electro-optical trap for dipolar excitons in a GaAs/AlAs Schottky diode with a single quantum well, Pis'ma Zh. Eksp. Teor. Fiz. **94**, 877 (2011) [JETP Lett. **94**, 800 (2011)].

[9] M. Alloing, A. Lemaître, E. Galopin, and F. Dubin, Nonlinear dynamics and inner-ring photoluminescence pattern of indirect excitons, Phys. Rev. B **85**, 245106 (2012).

[10] S. Lazić, A. Violante, K. Cohen, R. Hey, R. Rapaport, and P. V. Santos, Scalable interconnections for remote indirect exciton systems based on acoustic transport, Phys. Rev. B **89**, 085313 (2014).

[11] C. J. Dorow, M. W. Hasling, D. J. Choksy, J. R. Leonard, L. V. Butov, K. W. West, and L. N. Pfeiffer, High-mobility indirect excitons in wide single quantum well, Appl. Phys. Lett. **113**, 212102 (2018).

[12] S. Zimmermann, G. Schedelbeck, A. O. Govorov, A. Wixforth, J. P. Kotthaus, M. Bichler, W. Wegscheider, and G. Abstreiter, Spatially resolved exciton trapping in a voltage-controlled lateral superlattice, Appl. Phys. Lett. **73**, 154 (1998).

[13] M. Remeika, J. C. Graves, A. T. Hammack, A. D. Meyertholen, M. M. Fogler, L. V. Butov, M. Hanson, and A. C. Gossard, Localization-Delocalization Transition of Indirect Excitons in Lateral Electrostatic Lattices, Phys. Rev. Lett. **102**, 186803 (2009).

[14] M. Remeika, M. M. Fogler, L. V. Butov, M. Hanson, and A. C. Gossard, Two-dimensional electrostatic lattices for indirect excitons, Appl. Phys. Lett. **100**, 061103 (2012).

[15] X. P. Vögele, D. Schuh, W. Wegscheider, J. P. Kotthaus, and A. W. Holleitner, Density Enhanced Diffusion of Dipolar Excitons within a One-Dimensional Channel, Phys. Rev. Lett. **103**, 126402 (2009).

[16] K. Cohen, R. Rapaport, and P. V. Santos, Remote Dipolar Interactions for Objective Density Calibration and Flow Control of Excitonic Fluids, Phys. Rev. Lett. **106**, 126402 (2011).

[17] A. G. Winbow, J. R. Leonard, M. Remeika, Y. Y. Kuznetsova, A. A. High, A. T. Hammack, L. V. Butov, J. Wilkes, A. A. Guenther, A. L. Ivanov, M. Hanson, and A. C. Gossard, Electrostatic Conveyer for Excitons, Phys. Rev. Lett. **106**, 196806 (2011).

[18] C. J. Dorow, J. R. Leonard, M. M. Fogler, L. V. Butov, K. W. West, and L. N. Pfeiffer, Split-gate device for indirect excitons, Appl. Phys. Lett. **112**, 183501 (2018).

[19] A. A. High, E. E. Novitskaya, L. V. Butov, M. Hanson, and A. C. Gossard, Control of exciton fluxes in an excitonic integrated circuit, Science **321**, 229 (2008).

[20] G. Grosso, J. Graves, A. T. Hammack, A. A. High, L. V. Butov, M. Hanson, and A. C. Gossard, Excitonic switches operating at around 100 K, Nat. Photonics **3**, 577 (2009).

[21] D. S. Chemla, D. A. B. Miller, P. W. Smith, A. C. Gossard, and W. Wiegmann, Room temperature excitonic nonlinear absorption and refraction in GaAs/AlGaAs multiple quantum well structures, IEEE J. Quantum Electron. **20**, 265 (1984).

[22] K. Sivalertporn, L. Mouchliadis, A. L. Ivanov, R. Philp, and E. A. Muljarov, Direct and indirect excitons in semiconductor coupled quantum wells in an applied electric field, Phys. Rev. B **85**, 045207 (2012).

[23] A. Zrenner, P. Leeb, J. Schäfler, G. Böhm, G. Weimann, J. M. Worlock, L. T. Florez, and J. P. Harbison, Indirect excitons in coupled quantum well structures, Surf. Sci. **263**, 496 (1992).

[24] F. Chiaruttini, T. Guillet, C. Brimont, B. Jouault, P. Lefebvre, J. Vives, S. Chenot, Y. Cordier, B. Damilano, and M. Vladimirova, Trapping dipolar exciton fluids in GaN/(AlGa)N nanostructures, Nano Lett. **19**, 4911 (2019).

[25] A. K. Geim and I. V. Grigorieva, Van der Waals heterostructures, Nature (London) **499**, 419 (2013).

[26] Z. Ye, T. Cao, K. O'Brien, H. Zhu, X. Yin, Y. Wang, S. G. Louie, and X. Zhang, Probing excitonic dark states in single-layer tungsten disulphide, Nature (London) **513**, 214 (2014).

[27] A. Chernikov, T. C. Berkelbach, H. M. Hill, A. Rigosi, Y. Li, O. B. Aslan, D. R. Reichman, M. S. Hybertsen, and T. F. Heinz, Exciton Binding Energy and Nonhydrogenic Rydberg Series in Monolayer WS_2, Phys. Rev. Lett. **113**, 076802 (2014).

[28] M. M. Fogler, L. V. Butov, and K. S. Novoselov, High-temperature superfluidity with indirect excitons in van der Waals heterostructures, Nat. Commun. **5**, 4555 (2014).

[29] T. Deilmann and K. S. Thygesen, Interlayer trions in the MoS_2/WS_2 van der Waals heterostructure, Nano Lett. **18**, 1460 (2018).

[30] E. V. Calman, M. M. Fogler, L. V. Butov, S. Hu, A. Mishchenko, and A. K. Geim, Indirect excitons in van der Waals

heterostructures at room temperature, Nat. Commun. **9**, 1895 (2018).

[31] F. Wu, T. Lovorn, and A. H. MacDonald, Theory of optical absorption by interlayer excitons in transition metal dichalcogenide heterobilayers, Phys. Rev. B **97**, 035306 (2018).

[32] H. Yu, G.-B. Liu, and W. Yao, Brightened spin-triplet interlayer excitons and optical selection rules in van der Waals heterobilayers, 2D Mater. **5**, 035021 (2018).

[33] F. Wu, T. Lovorn, and A. H. MacDonald, Topological Exciton Bands in Moiré Heterojunctions, Phys. Rev. Lett. **118**, 147401 (2017).

[34] H. Yu, G.-B. Liu, J. Tang, X. Xu, and W. Yao, Moiré excitons: From programmable quantum emitter arrays to spin-orbit-coupled artificial lattices, Sci. Adv. **3**, e1701696 (2017).

[35] C. Zhang, C.-P. Chuu, X. Ren, M.-Y. Li, L.-J. Li, C. Jin, M.-Y. Chou, and C.-K. Shih, Interlayer couplings, Moiré patterns, and 2D electronic superlattices in $\mathrm{MoS_2/WSe_2}$ hetero-bilayers, Sci. Adv. **3**, e1601459 (2017).

[36] R. Bistritzer and A. H. MacDonald, Moiré butterflies in twisted bilayer graphene, Phys. Rev. B **84**, 035440 (2011).

[37] P. Rivera, H. Yu, K. L. Seyler, N. P. Wilson, W. Yao, and X. Xu, Interlayer valley excitons in heterobilayers of transition metal dichalcogenides, Nat. Nanotechnol. **13**, 1004 (2018).

[38] N. Zhang, A. Surrente, M. Baranowski, D. K. Maude, P. Gant, A. Castellanos-Gomez, and P. Plochocka, Moiré intralayer excitons in a $\mathrm{MoSe_2/MoS_2}$ heterostructure, Nano Lett. **18**, 7651 (2018).

[39] A. Ciarrocchi, D. Unuchek, A. Avsar, K. Watanabe, T. Taniguchi, and A. Kis, Polarization switching and electrical control of interlayer excitons in two-dimensional van der Waals heterostructures, Nat. Photonics **13**, 131 (2019).

[40] K. L. Seyler, P. Rivera, H. Yu, N. P. Wilson, E. L. Ray, D. G. Mandrus, J. Yan, W. Yao, and X. Xu, Signatures of moiré-trapped valley excitons in $\mathrm{MoSe_2/WSe_2}$ heterobilayers, Nature (London) **567**, 66 (2019).

[41] K. Tran, G. Moody, F. Wu, X. Lu, J. Choi, K. Kim, A. Rai, D. A. Sanchez, J. Quan, A. Singh, J. Embley, A. Zepeda, M. Campbell, T. Autry, T. Taniguchi, K. Watanabe, N. Lu, S. K. Banerjee, K. L. Silverman, S. Kim, E. Tutuc, L. Yang, A. H. MacDonald, and X. Li, Evidence for moiré excitons in van der Waals heterostructures, Nature (London) **567**, 71 (2019).

[42] C. Jin, E. C. Regan, A. Yan, M. Iqbal B. Utama, D. Wang, S. Zhao, Y. Qin, S. Yang, Z. Zheng, S. Shi, K. Watanabe, T. Taniguchi, S. Tongay, A. Zettl, and F. Wang, Observation of moiré excitons in $\mathrm{WSe_2/WS_2}$ heterostructure superlattices, Nature (London) **567**, 76 (2019).

[43] E. M. Alexeev, D. A. Ruiz-Tijerina, M. Danovich, M. J. Hamer, D. J. Terry, P. K. Nayak, S. Ahn, S. Pak, J. Lee, J. I. Sohn, M. R. Molas, M. Koperski, K. Watanabe, T. Taniguchi, K. S. Novoselov, R. V. Gorbachev, H. S. Shin, V. I. Fal'ko, and A. I. Tartakovskii, Resonantly hybridized excitons in moiré superlattices in van der Waals heterostructures, Nature (London) **567**, 81 (2019).

[44] C. Jin, E. C. Regan, D. Wang, M. Iqbal B. Utama, C.-S. Yang, J. Cain, Y. Qin, Y. Shen, Z. Zheng, K. Watanabe, T. Taniguchi, S. Tongay, A. Zettl, and F. Wang, Identification of spin, valley and moiré quasi-angular momentum of interlayer excitons, Nat. Phys. **15**, 1140 (2019).

[45] P. Rivera, J. R. Schaibley, A. M. Jones, J. S. Ross, S. Wu, G. Aivazian, P. Klement, K. Seyler, G. Clark, N. J. Ghimire, J. Yan, D. G. Mandrus, W. Yao, and X. Xu, Observation of long-lived interlayer excitons in monolayer $\mathrm{MoSe_2}$-$\mathrm{WSe_2}$ heterostructures, Nat. Commun. **6**, 6242 (2015).

[46] B. Miller, A. Steinhoff, B. Pano, J. Klein, F. Jahnke, A. Holleitner, and U. Wurstbauer, Long-lived direct and indirect interlayer excitons in van der Waals heterostructures, Nano Lett. **17**, 5229 (2017).

[47] M. Okada, A. Kutana, Y. Kureishi, Y. Kobayashi, Y. Saito, T. Saito, K. Watanabe, T. Taniguchi, S. Gupta, Y. Miyata, B. I. Yakobson, H. Shinohara, and R. Kitaura, Direct and indirect interlayer excitons in a van der Waals heterostructure of $\mathrm{hBN/WS_2/MoS_2/hBN}$, ACS Nano **12**, 2498 (2018).

[48] A. T. Hanbicki, H.-J. Chuang, M. R. Rosenberger, C. S. Hellberg, S. V. Sivaram, K. M. McCreary, I. I. Mazin, and B. T. Jonker, Double indirect interlayer exciton in a $\mathrm{MoSe_2/WSe_2}$ van der Waals heterostructure, ACS Nano **12**, 4719 (2018).

[49] E. V. Calman, L. H. Fowler-Gerace, D. J. Choksy, L. V. Butov, D. E. Nikonov, I. A. Young, S. Hu, A. Mishchenko, and A. K. Geim, Indirect excitons and trions in $\mathrm{MoSe_2/WSe_2}$ van der Waals heterostructures, Nano Lett. **20**, 1869 (2020).

[50] N. Kumar, Q. Cui, F. Ceballos, D. He, Y. Wang, and H. Zhao, Exciton diffusion in monolayer and bulk $\mathrm{MoSe_2}$, Nanoscale **6**, 4915 (2014).

[51] M. Kulig, J. Zipfel, P. Nagler, S. Blanter, C. Schüller, T. Korn, N. Paradiso, M. M. Glazov, and A. Chernikov, Exciton Diffusion and Halo Effects in Monolayer Semiconductors, Phys. Rev. Lett. **120**, 207401 (2018).

[52] F. Cadiz, C. Robert, E. Courtade, M. Manca, L. Martinelli, T. Taniguchi, K. Watanabe, T. Amand, A. C. H. Rowe, D. Paget, B. Urbaszek, and X. Marie, Exciton diffusion in $\mathrm{WSe_2}$ monolayers embedded in a van der Waals heterostructure, Appl. Phys. Lett. **112**, 152106 (2018).

[53] D. F. Cordovilla Leon, Z. Li, S. W. Jang, C.-H. Cheng, and P. B. Deotare, Exciton transport in strained monolayer $\mathrm{WSe_2}$, Appl. Phys. Lett. **113**, 252101 (2018).

[54] D. F. Cordovilla Leon, Z. Li, S. W. Jang, and P. B. Deotare, Hot exciton transport in $\mathrm{WSe_2}$ monolayers, Phys. Rev. B **100**, 241401(R) (2019).

[55] S. Hao, M. Z. Bellus, D. He, Y. Wang, and H. Zhao, Controlling exciton transport in monolayer $\mathrm{MoSe_2}$ by dielectric screening, Nanoscale Horiz. **5**, 139 (2020).

[56] P. Rivera, K. L. Seyler, H. Yu, J. R. Schaibley, J. Yan, D. G. Mandrus, W. Yao, and X. Xu, Valley-polarized exciton dynamics in a 2D semiconductor heterostructure, Science **351**, 688 (2016).

[57] L. A. Jauregui, A. Y. Joe, K. Pistunova, D. S. Wild, A. A. High, Y. Zhou, G. Scuri, K. De Greve, A. Sushko, C.-H. Yu, T. Taniguchi, K. Watanabe, D. J. Needleman, M. D. Lukin, H. Park, and P. Kim, Electrical control of interlayer exciton dynamics in atomically thin heterostructures, Science **366**, 870 (2019).

[58] D. Unuchek, A. Ciarrocchi, A. Avsar, Z. Sun, K. Watanabe, T. Taniguchi, and A. Kis, Valley-polarized exciton currents in a van der Waals heterostructure, Nat. Nanotechnol. **14**, 1104 (2019).

[59] Y. Liu, K. Dini, Q. Tan, T. Liew, K. S. Novoselov, and W. Gao, Electrically controllable router of interlayer excitons, Sci. Adv. **6**, eaba1830 (2020).

[60] Z. Huang, Y. Liu, K. Dini, Q. Tan, Z. Liu, H. Fang, J. Liu, T. Liew, and W. Gao, Robust room temperature valley Hall effect of interlayer excitons, Nano Lett. **20**, 1345 (2020).

[61] D. Unuchek, A. Ciarrocchi, A. Avsar, K. Watanabe, T. Taniguchi, and A. Kis, Room-temperature electrical control of exciton flux in a van der Waals heterostructure, Nature (London) **560**, 340 (2019).

[62] Y. Tang, L. Li, T. Li, Y. Xu, S. Liu, K. Barmak, K. Watanabe, T. Taniguchi, A. H. MacDonald, J. Shan, and K. F. Mak, Simulation of Hubbard model physics in $\mathrm{WSe}_2/\mathrm{WS}_2$ moiré superlattices, Nature (London) **579**, 353 (2020).

[63] D. M. Kennes, M. Claassen, L. Xian, A. Georges, A. J. Millis, J. Hone, C. R. Dean, D. N. Basov, A. N. Pasupathy, and A. Rubio, Moiré heterostructures as a condensed-matter quantum simulator, Nat. Phys. **17**, 155 (2021).

[64] G.-B. Liu, W.-Y. Shan, Y. Yao, W. Yao, and D. Xiao, Three-band tight-binding model for monolayers of group-VIB transition metal dichalcogenides, Phys. Rev. B **88**, 085433 (2013).

[65] G. Wang, C. Robert, A. Suslu, B. Chen, S. Yang, S. Alamdari, I. C. Gerber, T. Amand, X. Marie, S. Tongay, and B. Urbaszek, Spin-orbit engineering in transition metal dichalcogenide alloy monolayers, Nat. Commun. **6**, 10110 (2015).

[66] X.-X. Zhang, Y. You, S. Y. F. Zhao, and T. F. Heinz, Experimental Evidence for Dark Excitons in Monolayer WSe_2, Phys. Rev. Lett. **115**, 257403 (2015).

[67] Y. Zhou, G. Scuri, D. S. Wild, A. A. High, A. Dibos, L. A. Jauregui, C. Shu, K. De Greve, Kateryna Pistunova, Andrew Y. Joe, Takashi Taniguchi, Kenji Watanabe, Philip Kim, M. D. Lukin, and H. Park, Probing dark excitons in atomically thin semiconductors via near-field coupling to surface plasmon polaritons, Nat. Nanotechnol. **12**, 856 (2017).

[68] X.-X. Zhang, T. Cao, Z. Lu, Y.-C. Lin, F. Zhang, Y. Wang, Z. Li, J. C. Hone, J. A. Robinson, D. Smirnov, S. G. Louie, and T. F. Heinz, Magnetic brightening and control of dark excitons in monolayer WSe_2, Nat. Nanotechnol. **12**, 883 (2017).

[69] J. S. Alden, A. W. Tsen, P. Y. Huang, R. Hovden, L. Brown, J. Park, D. A. Muller, and P. L. McEuen, Strain solitons and topological defects in bilayer graphene, Proc. Natl. Acad. Sci. USA **110**, 11256 (2013).

[70] C. R. Woods, L. Britnell, A. Eckmann, R. S. Ma, J. C. Lu, H. M. Guo, X. Lin, G. L. Yu, Y. Cao, R. V. Gorbachev, A. V. Kretinin, J. Park, L. A. Ponomarenko, M. I. Katsnelson, Yu. N. Gornostyrev, K. Watanabe, T. Taniguchi, C. Casiraghi, H.-J. Gao, A. K. Geim, and K. S. Novoselov, Commensurate-incommensurate transition in graphene on hexagonal boron nitride, Nat. Phys. **10**, 451 (2014).

[71] H. Yoo, R. Engelke, S. Carr, S. Fang, K. Zhang, P. Cazeaux, S. H. Sung, R. Hovden, A. W. Tsen, T. Taniguchi, K. Watanabe, G.-C. Yi, M. Kim, M. Luskin, E. B. Tadmor, E. Kaxiras, and P. Kim, Atomic and electronic reconstruction at the van der Waals interface in twisted bilayer graphene, Nat. Mater. **18**, 448 (2019).

[72] A. Weston, Y. Zou, V. Enaldiev, A. Summerfield, N. Clark, V. Zólyomi, A. Graham, C. Yelgel, S. Magorrian, M. Zhou, J. Zultak, D. Hopkinson, A. Barinov, T. H. Bointon, A. Kretinin, N. R. Wilson, P. H. Beton, V. I. Fal'ko, S. J. Haigh, and R. Gorbachev, Atomic reconstruction in twisted bilayers of transition metal dichalcogenides, Nat. Nanotechnol. **15**, 592 (2020).

[73] M. R. Rosenberger, H.-J. Chuang, M. Phillips, V. P. Oleshko, K. M. McCreary, S. V. Sivaram, C. S. Hellberg, and B. T. Jonker, Twist angle-dependent atomic reconstruction and moiré patterns in transition metal dichalcogenide heterostructures, ACS Nano **14**, 4550 (2020).

[74] T. Korn, S. Heydrich, M. Hirmer, J. Schmutzler, and C. Schüller, Low-temperature photocarrier dynamics in monolayer MoS_2, Appl. Phys. Lett. **99**, 102109 (2011).

[75] A. Zrenner, L. V. Butov, M. Hagn, G. Abstreiter, G. Böhm, and G. Weimann, Quantum Dots Formed by Interface Fluctuations in AlAs/GaAs Coupled Quantum Well Structures, Phys. Rev. Lett. **72**, 3382 (1994).

[76] F. Withers, O. Del Pozo-Zamudio, A. Mishchenko, A. P. Rooney, A. Gholinia, K. Watanabe, T. Taniguchi, S. J. Haigh, A. K. Geim, A. I. Tartakovskii, and K. S. Novoselov, Light-emitting diodes by band-structure engineering in van der Waals heterostructures, Nat. Mater. **14**, 301 (2015).